Quaternary Research 80 (2013) 20–32

Contents lists available at SciVerse ScienceDirect

Quaternary Research

journal homepage: www.elsevier.com/locate/yqres

Characteristics of sea-cliff erosion induced by a strong winter storm in the eastern Mediterranean

Oded Katz, Amit Mushkin *

Geological Survey of Israel, 30 Malkhe Israel St., Jerusalem 95501, Israel

ARTICLE INFO

Article history:
Received 5 June 2012
Available online 24 May 2013

Keywords:
Coastal cliff
Erosion
Retreat
Extreme storm
LiDAR

ABSTRACT

Changes in sea-cliff morphologies along the 30-km-long Sharon Escarpment segment of Israel's weakly cemented Mediterranean eolianite cliff line were analyzed to gain quantitative insights into erosion characteristics associated with a high-energy winter storm (10–20 year return interval). Ground-based repeat LiDAR measurements at five sites along the cliff line captured perturbations of cliff stability by basal wave scouring during the storm, subsequent post-storm gravity-driven slope failures in the cliff face above, and return of the system to transient stability within several months. Post-storm erosion, which amounted to 70% of the total volume of cliff erosion documented, resulted in dramatic local effects of up to 8 m of cliff-top retreat. And yet, at the larger scale of the 30-km cliff line examined, erosion during the storm and the year that followed affected less than 4% of the cliff length and does not appear to be above the average cliff-length annual erosion implied by previously published decadal-scale retreat rates along this sea cliff. Our results do not support a direct association between strong storm events and elevated erosion and retreat at the cliff-line scale.

1. Introduction

Erosion and inland retreat of coastal cliffs present one of the most dynamic landscape evolution processes presently challenging coastal communities and infrastructure (e.g., Sunamura, 1992; Benumof et al., 2000; Moore and Griggs, 2002; Collins and Sitar, 2008). As such, and because of the potential acceleration of coastal cliff erosion in light of climatic changes and projected sea-level rise (Bray and Hoke, 1997; Zhang et al., 2004), the study of coastal cliff retreat has benefitted from a wealth of recent studies aimed at quantitatively characterizing the phenomenon and the time scales associated with it (e.g., Budetta et al., 2000; Lee et al., 2001, 2002; Dong and Guzzetti, 2005; Mills et al., 2005; Rosser et al., 2005; Collins and Sitar, 2008; Young et al., 2009a,b, 2011).

Historical to decadal sea-cliff retreat patterns have typically been studied using aerial photography and historical maps (e.g., Komar and Shih, 1993; Zviely and Klein, 2004; Teixeira, 2006; Marques, 2008; Brooks and Spencer, 2010; Brooks et al., 2012). For longer-term geologic time scales, quantitative estimates of Quaternary retreat rates are now emerging with the application of cosmogenic radionuclide dating techniques for constraining exposure histories in sea-cliff environments (e.g., Regard et al., 2012). Whereas these approaches provide important time-averaged constraints for the cumulative geomorphic effect of the suite of erosional processes that drive coastal cliff retreat, complementary investigations of sea-cliff activity at annual time scales and below (e.g., Allan and Komar, 2002; Hapke and Richmond, 2002; Sallenger et al., 2002; Ferreira, 2005) are also required to characterize the fundamental mechanisms that govern erosion in this environment.

Recent technological advances using airborne and terrestrial LiDAR scanning, which facilitate high resolution 3D mapping of sea-cliff morphologies, provide unprecedented resources to study the spatial distribution of sea-cliff activity and erosional processes at sub-annual time scales (e.g., Lim et al., 2005; Collins and Sitar, 2008; Young et al., 2009a,b; Lim et al., 2010; Quinn et al., 2010; Young et al., 2010; Olsen et al., 2011; Young et al., 2011; Barlow et al., 2012). Yet, such quantitative characterization of sea-cliff activity at sub-annual time scales (e.g., individual storms) remains a challenging task mainly due to the frequent sampling intervals required to capture such short duration, spatially heterogeneous and often non-linear natural phenomena. Consequently, sea-cliff erosion patterns associated with short-duration strong weather events and the role of such events in the overall evolution of coastal cliff environments present one of the more loosely constrained and controversial aspects of coastal cliff retreat (Williams, 1956; Steers et al., 1979; Thorne et al., 2007; Brooks et al., 2012). In addition to bearing on the 'universal' debate regarding catastrophic vs. gradational evolution of geomorphic systems (Wolman and Miller, 1960), constraining the role of extreme storms in the evolution of coastal cliffs also bears direct societal implications on cliff-retreat mitigation policies in light of projected climatic change, global sea-level rise and the potential increase in stormicity (e.g., Lowe et al., 2009).

In this study we used a sequence of 22 high-resolution (1–2 cm) ground-based LiDAR scans to quantify changes in cliff-face morphologies

* Corresponding author.
E-mail address: mushkin@gsi.gov.il (A. Mushkin).

0033-5894/$ – see front matter © 2013 Published by Elsevier Inc. on behalf of University of Washington.
http://dx.doi.org/10.1016/j.yqres.2013.04.004

at 5 selected sites along Israel's Mediterranean eolianite coastal cliff line during a 13-month period between Oct. 2010 and Nov. 2011. These data allowed us to identify and characterize the fundamental short-duration erosion processes that govern sea-cliff activity and retreat in response to a pronounced (10–20 year return period) high-energy winter storm event that occurred in the region on December 11–13, 2010. We present a case study that captures key elements of a sea-cliff erosion cycle characterized by 'instantaneous' perturbation in cliff stability induced by the storm, a subsequent peak in post-storm cliff erosion, and relaxation of the system down to transient stability. In addition, field mapping along a 30-km segment of the cliff line surrounding the 5 LiDAR sites allowed us to constrain the spatial distribution of storm-related erosion at the larger cliff-line scale.

1.1. The Sharon coastal cliff escarpment

A sequence of coast parallel, Nilotic, late Pleistocene to early Holocene eolianite ridges characterize Israel's Mediterranean coast line (Tsoar, 2000; Frenchen et al., 2001; Almagor, 2005; Fig. 1), which experienced ca. 7 km inland migration during the rapid post-LGM (last glacial maximum) Holocene sea-level rise of the eastern Mediterranean (Sivan et al., 2001; Lambeck and Purcell, 2005). Sea level in the region stabilized at ca. 3000 ^{14}C yr BP, after which less than 1 m of sea-level fluctuations have been documented (Sivan et al., 2004; Klein and Lichter, 2007). Thus, the present-day sea cliff that marks central Israel's Mediterranean coast has been formed through land–sea interaction since the late Holocene.

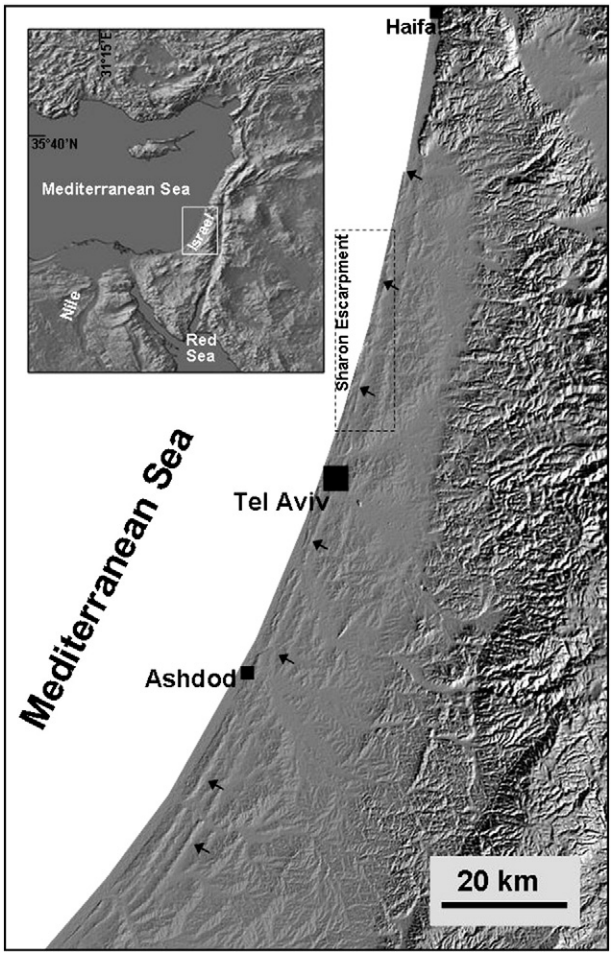

Figure 1. Location map of the studied Sharon coastal cliff Escarpment. Black arrows highlight the coast-parallel eolianite ridges that characterize Israel's Mediterranean coastal plain. Dotted rectangle is shown in Fig. 2.

Measured sea-cliff retreat rates in the region, which have been typically constrained over decadal time scales from historical aerial photography, are variable and range between 0.1 and 0.5 m/yr (Zviely and Klein, 2004; Katz et al., 2007 and references within).

We focus here on a fairly continuous 30-km-long cliff segment of Israel's Mediterranean sea cliff that lies in the Sharon region between Herzlia and Olga, termed herein as the 'Sharon Escarpment' (Fig. 2). The average height of the Sharon Escarpment is 18 m above sea level, and in places it reaches up to 50 m above sea level. The escarpment forms a generally linear NNE-striking geomorphic feature that is interrupted in only two places by the outlets of the Poleg and Alexander drainages. Perturbations in the plan-view linearity occur as capes and embayments up to hundreds of meters in length and tens of meters in amplitude. Capes are typically shielded by partially submerged boulder fronts and appear to be associated with increased mechanical strength of exposed cliff stratigraphy. Man-made cliff protection is minimal along the Sharon Escarpment and occurs in three places as: 1) Offshore man-made wave breakers that span 540 m at Natanya; 2) an ancient port and modern retaining wall that span ~150 m below the Apollonia archeological site; and 3) a recently emplaced retaining wall that spans 100 m just south of the Alexander drainage outlet (Fig. 2).

1.2. Cliff stratigraphy and hydrology

The cliffs of the Sharon Escarpment consists of alternating late Pleistocene–Holocene (Engelmann et al., 2001; Frenchen et al., 2001, 2002; Porat et al., 2004) quartz-dominated, carbonate-cemented eolianites and clay-bearing paleosols with common unconformable contacts (Yaalon, 1967; Gvirtzman et al., 1984) (Fig. 2). The lowermost Ramat Gan Eolianite is overlain by the Nahasholim paleosol. Dor Eolianite overlies the Nahasholim paleosol and is overlain by the Natanya paleosol, which is capped by the uppermost Tel Aviv Eolianite. The Ramat Gan and Dor eolianites are considered to be mechanically weak (Wiseman et al., 1981; Arkin and Michaeli, 1985; Frydman, 2011) and slope-failure type within these units is characteristic of weakly to moderately cemented sands as defined by Collins and Sitar (2011).

The regional groundwater level along the escarpment is less than 1 m above mean sea level (Shalev et al., 2009). Cliff-face exposures are therefore effectively situated above the groundwater level and within the unsaturated zone. There is no evidence indicating the existence of perched aquifers near the cliff face and spring discharges do not occur along the escarpment, even during the winter season. Maximum–minimum differences in tidal effects along the escarpment do not exceed 0.5 m. Waves traverse the typical sandy shores and reach the cliff base only during winter storms.

1.3. LiDAR study sites

Five separate 60–250 m long cliff segments were selected to represent the variability in cliff morphologies and exposed stratigraphy along the 30 km of the Sharon Escarpment (Fig. 3). Prior to the December 2010 storm, the cliffs at all sites were sub-vertical to vertical and were characterized by a well-developed crusted cliff-face appearance that indicated relative pre-storm stability.

I. *Olga South:* The monitored cliff segment here is 150 m long, rises up to 25 m above sea level and is composed primarily of Dor Eolianite. This site is located along a local cape that deviates up to 50 m seawards from the general NNE linear trend of the cliff line (Fig. 3A). Pre-storm conditions at the site (measured 47 days before the storm) presented a near-vertical cliff face and a beach stretch up to 10-m-wide interrupted midway by a pile of talus material associated with an older 20-m-long landslide scarp in the cliff face directly above. The north part of this site was shielded by partially submerged 0.5–3 m Dor Eolianite boulders that form two discrete fronts, located ~30

https://doi.org/10.1016/j.yqres.2013.04.004 Published online by Cambridge University Press

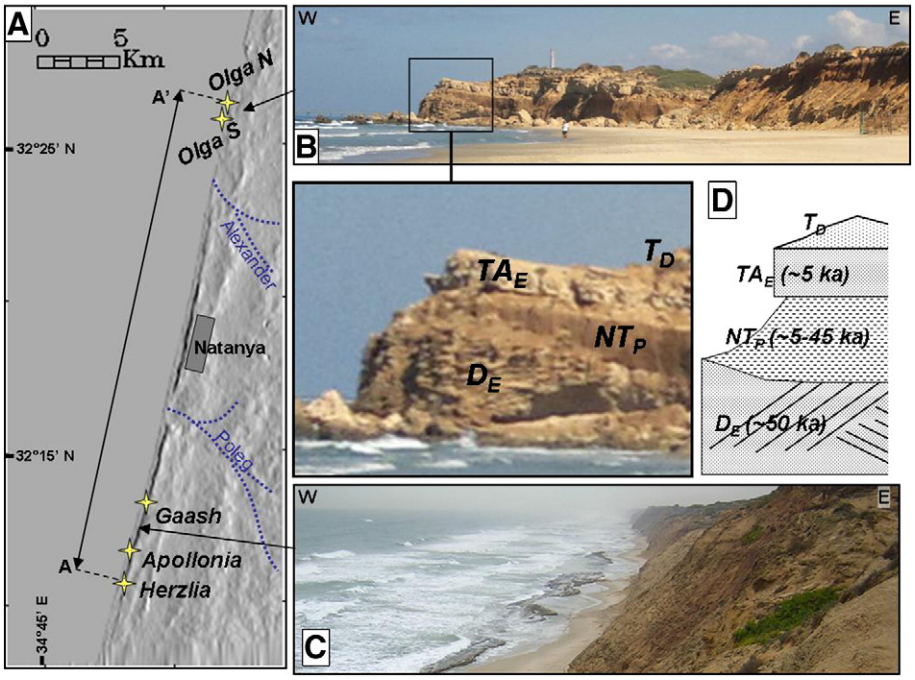

Figure 2. The Sharon Escarpment, between Herzlia and Olga N. (A) Location of the five LiDAR study sites along Sharon Escarpment. A and A′ mark the 30-km-long transect in Fig. 6. (B) Local capes and embayments occur along the generally linear NNE trending cliff line (C). (D) A generalized cross-section as exposed at a cape just south of the Olga S site: D_E — Dor Eolianite, NT_P — Natanya paleosol, TA_E — Tel-Aviv eolianite and T_D — active Ta'arukha dunes. The lower Nahsholim paleosol and Ramt-Gan eolianite are not exposed here.

and 45 m seawards of the cliff (Fig. 3A) and most likely represent two older cliff-collapse episodes.

II. *Olga North*: This monitored cliff segment is 60 m long, reaches a height of up to 20 m above sea level and is composed primarily of Dor Eolianite. The entire site is located at the apex of a prominent cape that deviates up to 50 m seawards from the general NNE linear trend of the cliff line. Similar to the Olga S site located ~1.5 km to the south, a near-vertical cliff face and a ~15-m-wide sandy beach stretch shielded by two discrete fronts of partially submerged boulders, ~25 and 40 m seaward of the cliff, characterized the pre-storm conditions at this site (Fig. 3B).

III. *Gaash*: The monitored cliff segment here is 260 m long and reaches up to 40 m above sea level. The base of the cliff is composed of the Ramat Gan Eolianite and is overlain by the Nahasholim paleosol, which itself is overlain by a ~20-m-thick section of the Dor Eolianite (Fig. 3C). Pre-storm conditions at this site (measured 27 days before the storm) presented a ~45° cliff face for the Dor Eolianite exposures and numerous talus piles (derived from the upper Dor Eolianite material) up against the basal Ramat Gan Eolianite, which exhibited near vertical cliff geometry, where exposed. A large 60-m-long talus (T_1), associated with an older landslide within the Dor Eolianite marked the middle of the studied stretch. The Gaash site was also characterized by a ~30-m-wide pre-storm sandy beach that separated the cliff base from the water line.

IV. *Apollonia*: This monitored cliff segment is 80-m-long, reaches up to 20 m above sea level and is composed primarily of the Ramat Gan Eolianite (Fig. 3D). Pre-storm conditions (measured 14 days before the storm) presented near-vertical cliffs with common cantilevered notches at the base and a narrow beach stretch up to 5 m wide that separated the cliff base from the water line.

V. *Herzlia*: The monitored cliff segment is 180-m-long, reaches a height of up to 25 m above sea level and is composed primarily of the Dor Eolianite. The pre-storm LiDAR survey at this site (conducted 42 days before the storm) documented a near-vertical cliff face with common basal talus piles (Fig. 3E) and a wide ~30 m sandy beach that separated the cliff base from the water line.

1.4. Regional climate and the December 2010 storm

The climate in the study area is Mediterranean with dry summers (June–August) and rainy winters (December–April). Average annual precipitation in the region is ca. 550 mm/yr (Goldreich, 2003). The highest concentration of rain days typically occurs between December and February. In terms of precipitation the 2010–2011 winter was an average season, with a total annual precipitation of 430 mm between 10/2010 and 9/2011. The December 2010 storm, which is the focus of this study, was the first major weather event in the 2010–2011 winter season and was recorded as an exceptionally strong high-energy meteorological event that lasted for three days between December 11 and 13, 2010 (Fig. 4). Precipitation during the storm amounted to 61 mm and peak wind speeds reached 21 m/s. Wave-height records at the Haifa and Ashdod ports (~40 km north and south of the escarpment, respectively) reveal maximum wave heights of 14 and 12 m, respectively, during the storm. The recurrence interval of such wave heights along the eastern Mediterranean shoreline is 20 and 10 years, respectively (Dr. M. Glozman, personal com., CAMERI: http://cee.technion.ac.il/eng/).

2. Approach and methodology

Israel's Mediterranean coastal cliff has been previously highlighted as an example for sea-cliff erosion in weakly cemented eolianite sea-cliff environments (e.g., Arkin and Michaeli, 1985; Collins and Sitar, 2011). Our experimental setup was designed to characterize the suite of physical processes that drive sea-cliff erosion and retreat along the Sharon Escarpment through high-resolution repeat ground-based LiDAR scans of cliff-face morphologies during the course of a year. As cliff-base erosional activity appears to have a key role in the evolution of weakly cemented coastal cliffs (Richards and Lorriman,

https://doi.org/10.1016/j.yqres.2013.04.004 Published online by Cambridge University Press

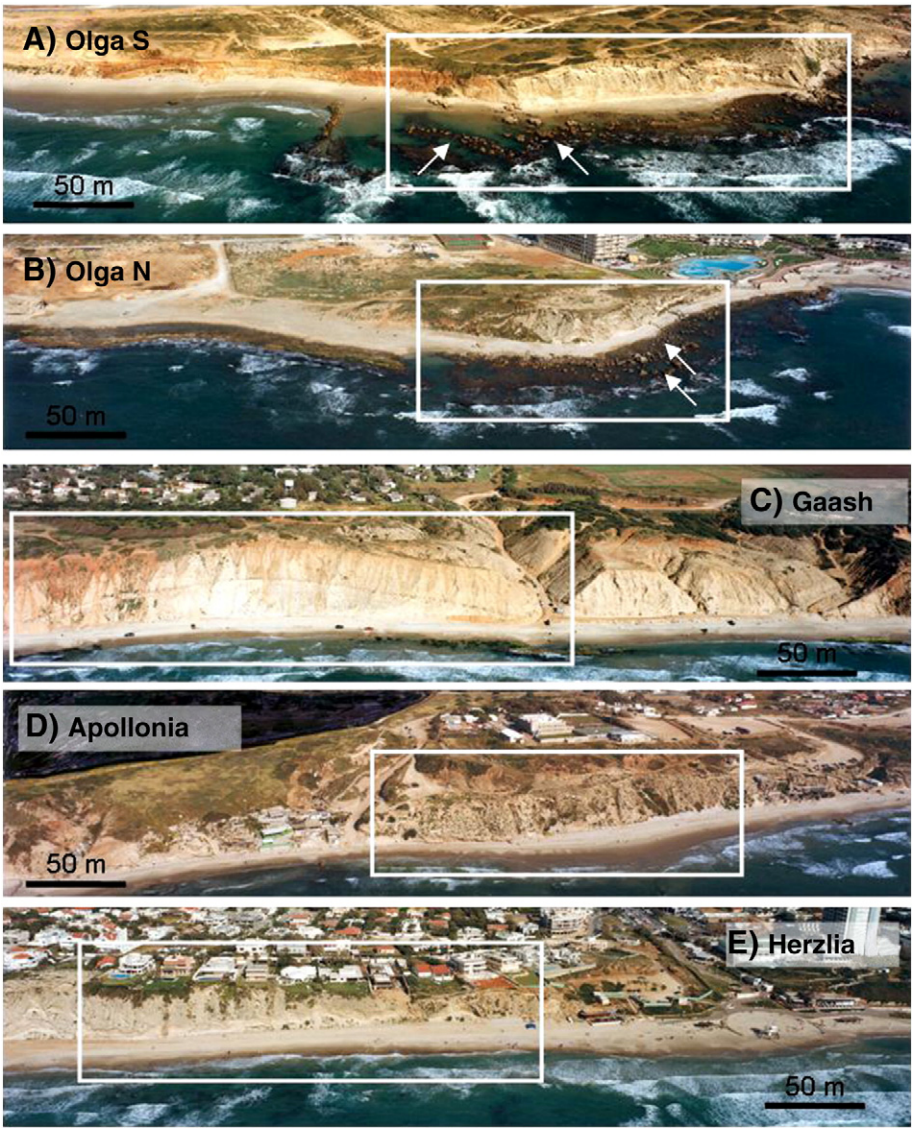

Figure 3. Oblique aerial photos of the LiDAR study sites. White boxes mark the scanned area within each site. Partially submerged boulder fronts that effectively shield local capes from erosion at Olga N and Olga S are highlighted by white arrows. Note the sandy beach stretch that typically separates the cliff base from the water line along the escarpment. This separation is maintained during daily tidal variations and is overcome only during winter storms.

1987; Jones et al., 1993; Collins and Sitar, 2008; Young and Ashford, 2008; Budetta, 2011), we used a ground-based LiDAR to accurately measure the steep and locally overhanging sea-cliff topography (Rosser et al., 2005; Young et al., 2010).

Recent slope failures along the Sharon Escarpment are readily identified in the field according to the "fresh" field appearance of their scars, which contrasts the “crusted” appearance of stable cliff exposures (Fig. 1Sa). Moreover, examination of scars associated with documented slope failures from previous years reveals a qualitative correlation between the age of the slides and the degree of progressive crusting and/or darkening that occurs at the surface of the eolianite exposures within the scar: the older the scar is, the more developed the crusting becomes. Therefore, the 2010–2011 cliff-collapse scars were easily distinguishable in the field according to their “fresh” non-crusted appearance, whereas stable cliff sections were readily identified according to their dark and “crusted” appearance. Accordingly, LiDAR-based mapping of changes in cliff-face morphologies were not utilized for identifying erosion associated with the storm, but rather for measuring the volume and 3D geometry of erosional activity independently identified as such through field-based observations.

2.1. Ground-based LiDAR surveys

LiDAR scans were carried out using a tripod-mounted Leica ScanStation2. A total of 22 surveys were conducted at the five sites over a period of 398 days from Oct. 21 2010 to Nov. 28, 2011. Scan resolution was typically less than 2 cm (sampling intervals projected onto the cliff face). Pre-existing stable structures (typically man-made) found within scan range were used as benchmarks for co-registration of surveys from different dates (‘epochs’) and were scanned at 0.3-cm resolution. The monitored cliff sections at each site were scanned from at least two positions (per epoch) in order to address inherent “shadowing” that commonly leads to data voids in rough natural surfaces. Scanner distances from the cliff were dictated by the position of the water line during measurements and ranged between 10 and 40 m. To avoid overly oblique point reflections an effort was made to avoid scanning angles larger than 45° with respect to the cliff.

Processing of the point-cloud data was carried within the ‘Cyclone’ software package (http://hds.leica-geosystems.com). At each site, co-registration of the vector data from the different epochs into a common coordinate system was followed by conversion into 7–

https://doi.org/10.1016/j.yqres.2013.04.004 Published online by Cambridge University Press

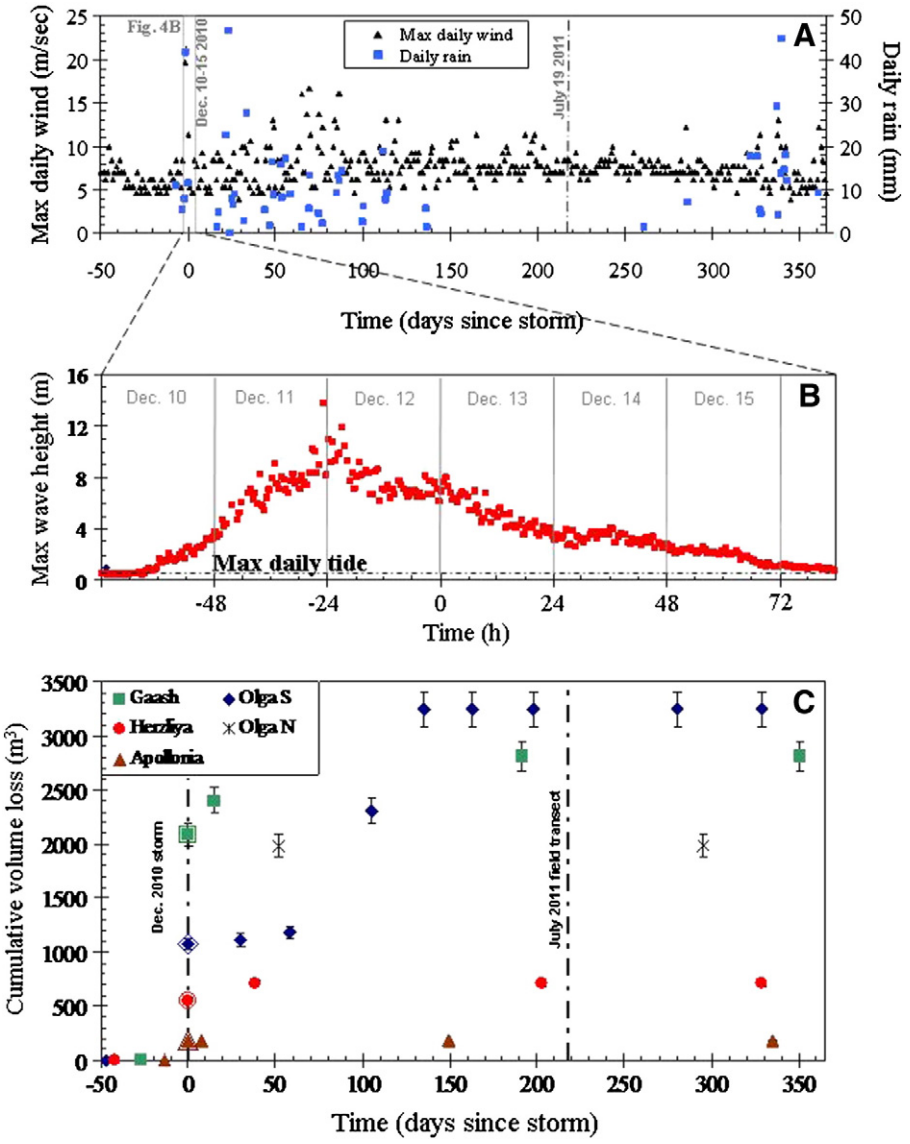

Figure 4. (A) Maximum daily wind and daily precipitation during the 2010–2011 season, from 50 days before until 1 year after the December 11–13 storm. Measurements were obtained from the Yedidya meteorological station located 5 km inland of Natanya. (B) Maximum wave heights at the Haifa port located 40 km north of the Sharon Escarpment (source: http://www.israports.org.il). Dotted line marks the maximum magnitude of tidal variations along the escarpment. (C) Cumulative volume loss from the cliff face at each site as function of time. Values along the x-axis are plotted according to the respective dates of the 22 LiDAR surveys conducted. Syn-storm erosion volumes were constrained from the first available post-storm LiDAR surveys at each site and are projected onto the 'storm line' as double framed markings. Uncertainty bounds for all volume estimates are ±6%.

12 cm/pixel grids using the ENVI commercial software package. A vertical (cliff-normal) reference plane was used to accommodate vertical and overhanging cliff morphologies. Cliff-normal difference maps were produced by subtracting co-registered grids from subsequent epochs. Erosion volumes were measured directly from these cliff-normal difference maps. Because the base of collapsed areas was commonly covered by talus and/or boulders, calculated erosion volumes are minimum values in most cases.

Accuracy for this change detection methodology was assessed by analyzing the apparent change measured with the LiDAR data within stable cliff sections, independently identified as such in the field according to their heavily crusted appearance. Two such stable ≥ 1 m^2 sections (i.e., >64 pixels each) were examined for each difference map that was produced. Detection limits were obtained by examining the apparent changes in these stable sections and were typically ±8 cm in the cliff-normal direction. As the cliff-failure events documented with the LiDAR resulted in average cliff-normal retreat larger than 150 cm we assume a conservative ±6% error in the erosion volumes reported herein. The LiDAR scans were used to quantify storm related cliff erosion, independently identified as such according to the characteristic fresh field appearance of failure scars, rather than for identifying the actual occurrence of such erosion. Thus, we regard the accuracy obtained as sufficient for the 1st-order characterization of the cliff erosion mechanisms discussed herein.

In our analysis we distinguish between cliff erosion that occurred during the storm and post-storm erosion, which refers to all forms of cliff erosion that occurred after the end of the storm on December 13, 2010. This distinction was based on field observations documenting the presence of or lack of intact, non-truncated tapering talus material below the eroded cliff face during the first post-storm survey at each site. All sites (except Olga N) were surveyed soon after the storm and before the next high-energy weather event, which occurred 48 days after the storm (Fig. 4). Thus, fresh collapse scars in the cliff face without associated collapse sediments (e.g., talus) below them (in the first post-storm survey) are categorized as 'syn-storm' activity with the assumption that these sediments were removed from the cliff base

https://doi.org/10.1016/j.yqres.2013.04.004 Published online by Cambridge University Press

during the storm itself. Accordingly, collapse scars with associated intact and non-truncated talus material directly below them were categorized as post-storm activity.

At the LiDAR sites we make another field-based distinction between erosion/removal of disintegrated 'loose' basal sediments, i.e., talus, and erosion of 'intact' cliff material. Accordingly, herein "talus erosion" relates to removal of material from pre-existing talus piles at the toe of the cliff and "cliff-face erosion" relates to removal of material from the cliff itself.

2.2. Sharon Escarpment field transect

A detailed field transect of storm-related cliff-face erosion along the entire Sharon Escarpment was conducted seven months after the December 2010 storm, on July 19, 2011. Cliff-face erosion scars from 2010 to 2011 were identified according to their "fresh" field appearance (see Section 2.1) and their locations were registered using a GPS receiver. The erosional volume marked by each of these scars was constrained according to estimates of its length, height and average cliff-normal depth. Comparison between volume constraints derived from these estimates and LiDAR measurements of slope failures at the LiDAR sites revealed up to 50% error in the non-LiDAR field-based volume estimates.

3. Results

3.1. Olga South

Cliff activity at this site was characterized with 9 post-storm LiDAR surveys (up to 329 days after the storm; Table 1) that documented a total of 3249 m^3 of erosion (Figs. 4 and 5). The first post-storm LiDAR survey was carried out 30 days after the storm and revealed extensive erosion along 95% of the studied cliff stretch. Cliff-face erosion during the storm (st_{1-3}, Fig. 5F) totaled 933 m^3 and was concentrated in the basal half of the cliff north of the pre-existing talus pile (st_4), which itself experienced 140 m^3 of erosion during the storm. Storm activity was terminated by deposition of a 1-m-high berm of eolianite cobbles (st_T) at the base of the cliff north of st_4. Post-storm activity up until the first survey was fairly minor totaling 41 m^3 as one rockfall event (P_1) that occurred at the southern end of the site.

The second post-storm LiDAR survey, conducted 58 days after the storm, documented a single 67 m^3 rockfall event (P_2) that occurred mid-cliff at the northern end of the site. The third post-storm LiDAR survey, conducted 105 days after the storm, recorded a massive 1128 m^3 rockfall event (P_3) that occurred on day 96 (March 19th personal comm. with local residents) just above st_1 and P_2. The fourth post-storm LiDAR survey, conducted 135 days after the storm, recorded another massive 940 m^3 rockfall event (P_4) that occurred between days 105 and 119 after the storm (personal comm. with local residents) above st_2. The P_3 and P_4 collapse events affected the entire cliff face and resulted in up to 8 m of inland cliff-top retreat. The remaining 4 post-storm LiDAR surveys at this site documented little change and overall cliff stability since the P_4 event. Nonetheless, prominent cliff-parallel fractures visually apparent ~2 m inland from the cliff face, within P^*_5 and P^*_6 place these cliff sections at elevated hazard for future collapse (Fig. S1).

3.2. Olga North

The first post-storm LiDAR survey, conducted 52 days after the storm (Fig. 4), recorded a massive 1985 m^3 post-storm rockfall (P_1; Fig. S2) that occurred on January 14th 2011, 33 days after the storm (reported on the local news). This rockfall affected the entire cliff height and resulted in 7 m of estimated inland cliff-top retreat. The second post-storm LIDAR survey at this site was conducted 295 days after the storm and documented little change and overall cliff stability since the P_1 event. A detached and tilted, yet still upright and intact, 10-m-high block (P^*_2; 300 m^3) is nested along the northern scarp of this rockslide. Field relations indicate that P^*_2 was detached from the cliff together with P_1 and therefore belongs to the same January 14th 2011 collapse event. The non-crusted "fresh" appearing ~1 m deep basal notch at the bottom of P^*_2 and along the cliff face just north of it indicates that basal erosion during the storm did in fact precede the January 14 collapse. Pre-storm LiDAR data are not available for this site.

Table 1
Summary of landslide volumes mapped in the five LiDAR sites.

Site	Location[a] (km)	Event[b]	Date[c]	Volume (m^3)	Remarks
Olga North	29.26	P_1	23	1985	–
Olga South	27.88	st1	0	257	
	27.93	st2	0	515	
	27.95	st3	0	161	
	27.97	st4	0	140	Talus erosion
	28.01	P_1	30	41	–
	27.87	P_2	58	67	st_1[d] – 44 m^3
	27.89	P_3	105	1128	st_1[d] – 218 m3
	27.91	P_4	135	940	St_2[d] – 272 m3
Ga'ash	5.50	st1	0	167	Talus erosion
	5.44	st2	0	274	Talus erosion
	5.38	st3	0	213	Talus erosion
	5.30	st4	0	607	Talus erosion
	5.22	st5	0	165	Talus erosion
	5.12	st6	0	665	Talus erosion
	5.36	P_1	15	141	st_3[d] – 87 m3
	5.07	P_2	15	171	st_6[d] – 73 m3
	5.44	P_3	191	155	st_1[d] – 90 m3
	5.38	P_4	191	31	st_2[d] – 28 m3
	5.36	P_5	191	204	st_{3-4}[d] – 428 m3
	5.21	P_6	191	18	st_5[d] – 13 m3
Apollonia	1.16	st1	0	4	
	1.14	st2	0	35	
	1.08	st3	0	13	
	1.07	St4	0	127	
	1.10	P_1	8	25	st_2[d]
	1.08	P_2	149	38	st_3[d] – 13 m3
Herzliya	0.15	St0	0	35	
	0.09	st1	0	296	Talus erosion
	0.03	st2	0	208	Talus erosion
	0.00	st3	0	51	Talus erosion
	0.15	P_1	38	155	st_1[d] – 52 m3
Total			8997/6211		w/o talus erosion

– Pre-storm data not available.
[a] Distance along the Sharon Escarpment (A–A′, shown in Fig. 2).
[b] Discrete erosion events, where *st* and *P* are syn- and post-storm events, respectively.
[c] Days after December 13, 2010. This value is the LiDAR surveying date and is a maximum time constraint for the failure event).
[d] Associated basal cliff erosion.

3.3. Gaash

The first post-storm LiDAR survey was conducted 15 days after the storm (Fig. 4) and recorded extensive storm erosion that affected >95% of the cliff length (Fig. S3, st_{1-6}). This erosion removed 2090 m^3 (Table 1) — primarily pre-existing talus material from the bottom 10 m of the cliff. Post-storm erosion at this site up until 15 days after the storm occurred as two discrete slumps ($P_{1,2}$) that totaled 312 m^3. Large parts of the sandy beach stretch were covered by a layer of eolianite pebbles, up to 0.5 m thick. The second post-storm LiDAR survey, conducted 191 days after the storm, documented post-storm erosion of 409 m^3 distributed between: a) two slumps ($P_{3,4}$; 155, 31 m^3, respectively) in the north, b) numerous smaller-scale slides (P_5) that total 204 m^3 within T_1 and c) several small-scale basal slides (P_6) within Ramat Gan Eolianite exposures in the south (total 18 m^3). The third post-storm LiDAR survey conducted 351 days after the storm revealed no significant change and overall cliff stability.

https://doi.org/10.1016/j.yqres.2013.04.004 Published online by Cambridge University Press

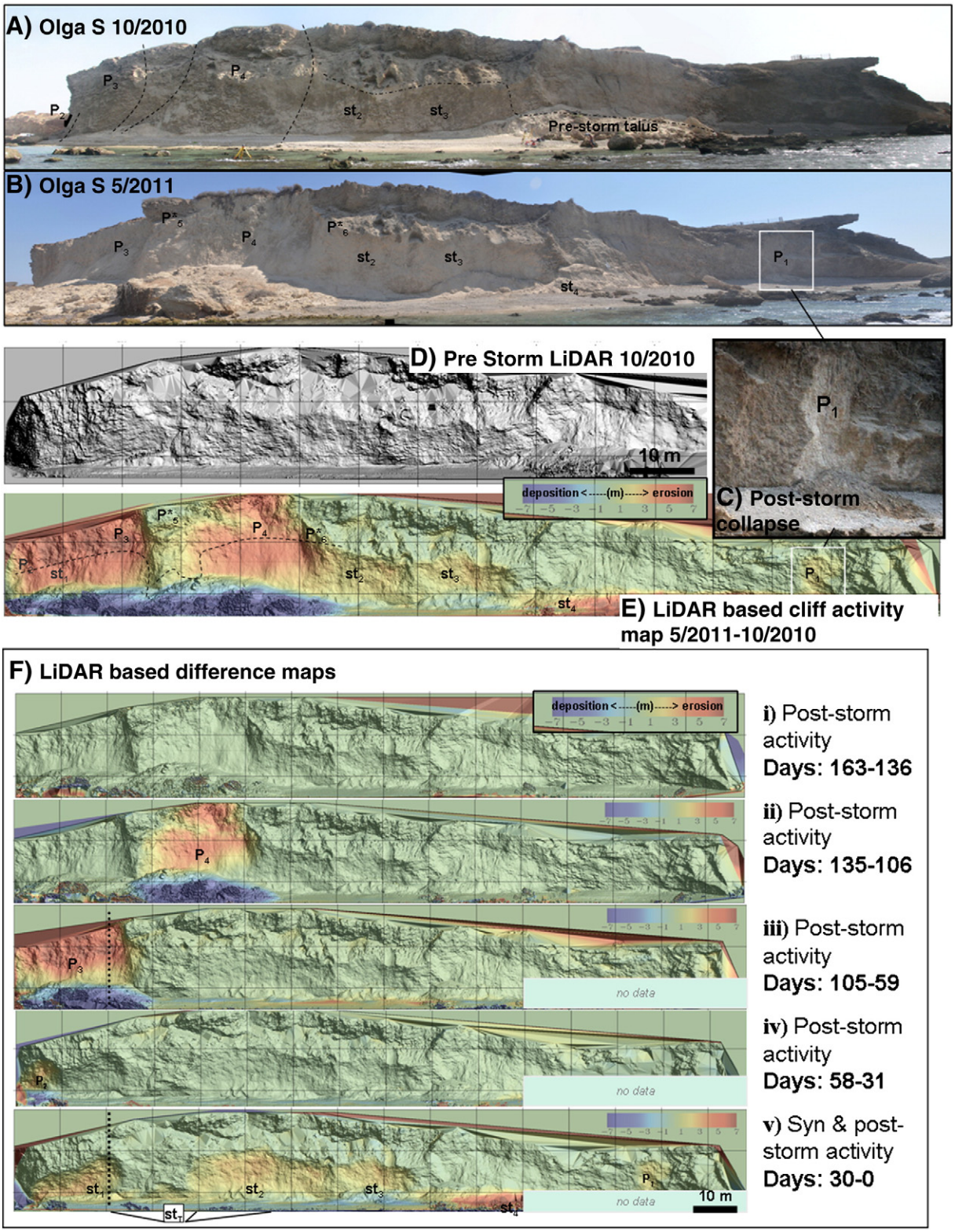

Figure 5. Olga South (A) pre-storm panorama. Dashed lines outline the locations of syn-storm (st) and post-storm (P) erosion along the cliff face. (B) Post-storm panorama. (C) Post-storm cliff failure marked by a basal talus pile below the collapse scar. Note the contrast between the "fresh" appearance of the cliff face inside the collapse scar and crusted and appearance of the stable cliff face outside the collapse scar. Note the non-truncated tapering appearance of the talus pile, which indicates that waves did not reach this elevation since the collapse event. (D) Pre-storm shaded relief map of the cliff face (10 cm/pixel); (E) shaded relief map of the cliff face (10 cm/pixel) showing cumulative cliff activity up to May 2011. (F) Shaded relief maps (10 cm/pixel) showing incremental cliff activity up until day 163 after the storm as incremental difference maps overlain onto shaded relief images of the cliff. Dotted vertical lines mark the location of the cross sections in Fig. 7. The four subsequent surveys preformed at this site after day 163 (not shown) revealed no significant changes in cliff morphology.

https://doi.org/10.1016/j.yqres.2013.04.004 Published online by Cambridge University Press

3.4. Apollonia

The first post-storm LiDAR survey conducted 8 days after the storm (Fig. 4) recorded syn-storm erosion of basal notches along ~90% of the cliff length (up to 4 m above sea-level) that totaled 52 m^3. In places 2–3 m deep basal notches were excavated (Fig. S4, st_{1-3}). The end of storm activity at this site was marked by deposition of a massive 1.5-m-high berm of eolianite pebbles and cobbles at the base of the entire cliff section and within the basal notches as well. The post-storm beach stretch separating the cliff base from the water line was effectively diminished to less than 2 m width. Post-storm erosion up until 8 days after the storm occurred as a single 10-m-high 127 m^3 rockfall (P_1) at the center of the site. The next post-storm LiDAR survey conducted on day 149 after the storm documented a single rockfall event (P_2, 38 m^3) at the south. The berm deposited during the storm was largely removed during this time period and the beach returned to its pre-storm width of ~5 m. The next post-storm survey conducted on day 335 after the storm revealed insignificant changes and overall cliff stability.

3.5. Herzlia

The first post-storm LiDAR survey conducted 38 days after the storm (Fig. S5) revealed syn-storm erosion of 555 m^3 from pre-existing basal talus piles (<3 m high) and a single post-storm rockfall event (P_1; 155 m^3). Two additional post-storm surveys were carried out 203 and 329 days after the storm and revealed insignificant changes and overall post-storm cliff stability.

3.6. Sharon Escarpment

79 discrete erosional scars associated with collapse events that occurred during the 2010–2011 season were identified and mapped along the Sharon Escarpment cliff face (Fig. 6; Table 2). The average volume of these discrete erosional events together with those documented at the 5 LiDAR sites (Tables 1 and 2) was 126 ± 251 m^3 and their total cliff-parallel length was less than 1 km, which is 3.3% of the Sharon Escarpment length.

4. Discussion

4.1. Cliff erosion associated with the storm

Cliff erosion during the storm at each of the monitored sites was consistently limited to the basal sections of the cliff and typically resulted in over steepened/basal notch — overhanging cliff geometry

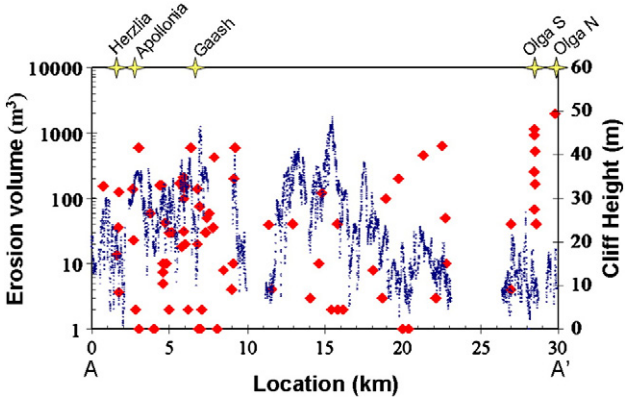

Figure 6. Cliff-face heights along the Sharon Escarpment (blue dots) and location and volume of the discrete cliff-face erosion events mapped along the escarpment during the study period (red diamonds).

(Figs. 5 and 7). Our observations do not provide direct evidence for distinguishing between the common forcing conditions for such sea-cliff erosion, i.e., groundwater, precipitation and/or wave scouring activity. However, the approximate sea-level elevation of the regional groundwater table (Shalev et al., 2009), lack of perched aquifers, and lack of groundwater discharge springs along the escarpment all suggest insignificant contribution of groundwater activity to cliff erosion. Top-down forcing of cliff erosion from precipitation also appears to be less likely due to the concentration of syn-storm erosion solely along the basal sections of the cliff. Thus, scouring driven by direct wave impact remains as the most likely mechanism for erosion during the storm. Wave scouring is also consistent with the distinct upper bound for storm erosion at each of the LiDAR sites as well as the basal notch cliff geometry carved in many places during the storm. In this context, hydraulic fracturing and direct fracturing by wave impact have been previously reported as effective rock-disintegrating mechanisms in coastal environments (Collins and Sitar, 2008; Hansom et al., 2008). Removal of material via wave action appears to also be the most likely mechanism for the extensive talus erosion documented at the LiDAR sites during the storm.

Post-storm erosion at the LiDAR sites started within 8 days after the storm and continued to occur as discrete slope failure events until 4 months after the storm (Fig. 4). The physical mechanisms of these post-storm collapse events and the resulting slope failure type varied with a marked dependence on local geology: rockfalls governed post-storm cliff-face erosion at sites where the cliff consists primarily of the Dor Eolianite (Olga S, Olga N, Apollonia and Herzlia). Prominent cliff-parallel tension cracks observed within destabilized Dor Eolianite cliff sections indicate that tensile failure was also likely involved. It also appears that these large rockfalls may occur through initial detachment of massive intact blocks, followed by disintegration of the blocks into large boulders and talus material during the rock slide event. Slumping, induced by basal instability initiated within the clay-rich Nahsholim paleosol, characterized the more heterogeneous cliff exposures displaying 'layered' geo-mechanical properties, such as at Gaash (Fig. 7).

Regardless of collapse mechanism and exposed lithologies, we find a correlation between post-storm up-cliff instability and basal cliff-face erosion during the storm directly below (Table 1): 13 of the 14 post-storm cliff collapses documented with the LiDAR data at the five study sites were preceded by measurable basal storm erosion of the cliff face directly below. This spatial correlation could not be established for only one case, due to lack of pre-storm LiDAR data for the small P_1 collapse at Olga S (Fig. 5).

Extensive talus erosion (2785 m^3; Table 1) through wave scouring during the storm characterized significant cliff sections within the monitored sites. Yet, the cliff itself above these sections did not experience erosion during the monitored period. Thus, as documented in other retreating sea cliffs, basal talus piles in the Sharon Escarpment appear to have a key role in sustaining transient cliff stability above, as they effectively shield the cliff base from direct wave impact and scouring during storms (Hapke and Richmond, 2002).

Our observations suggest that storm-driven erosion by waves at the base of the cliff cause post-storm gravitational instability of the cliff face above — an erosion sequence previously described for other weakly cemented sea cliffs, such as England's coast (Quinn et al., 2009; Brooks et al., 2012), California's pacific coast (Hampton, 2002; Hapke and Richmond, 2002; Young et al., 2011), Japan (Kogure et al., 2006; Kogure and Matsukura, 2010) and Italy (Budetta, 2011). Thus, the LiDAR measurements presented herein provide quantitative constraints for sea-cliff erosion sequences in which overhanging/oversteepened/basal-notch cliff geometry formed during strong storms potentially leads to a gravitationally unstable state that can promote subsequent gravity-driven slope failures in the cliff face above (e.g., Sunamura, 1982; Richards and Lorriman, 1987; Jones et al., 1993; Hampton, 2002). Within the limits of the temporal

https://doi.org/10.1016/j.yqres.2013.04.004 Published online by Cambridge University Press

Table 2
Summary of landslide volumes mapped along the Sharon Escarpment 218 days after the storm (l, h and t are landslide's scar length, height and cliff-normal depth, respectively).

Location[a] (km)	L (m)	h (m)	t (m)	Volume[b] (m^3)
2.03	10	7	2	140
2.13	5	3	1.5	22.5
2.23				2
2.43				1
2.44	50	6	2	600
2.45				1
3.23	20	3	1	60
3.42				1
3.43				1
3.44				1
3.79	20	8	1	160
3.82	20	8	1	160
3.85	20	8	1	160
3.88	20	8	1	160
3.91	20	8	1	160
3.99	10	1	0.5	5
4.005	10	2	0.5	10
4.02	10	1	0.5	5
4.03	5	3	0.5	7.5
4.13	7	3	2	42
4.23	5	2	1	10
4.43				2
4.44	10	3	1	30
4.53	10	3	1	30
4.58	10	3	1	30
5.33	10	10	1	100
5.43	10	2	1	20
5.62				2
5.63				2
5.83	20	10	3	600
6.22	4	5	1	20
6.23	10	7	2	140
6.32				1
6.33	10	5	1.5	75
6.44				1
6.44				1
6.45				1
6.45				1
6.46				1
6.46				2
6.73	5	6	1	30
6.83	10	5	1	50
6.93	10	6	1	60
7.24	7	5	1	35
7.25	7	5	1	35
7.26	7	5	1	35
7.33	20	7	3	420
7.53				1
7.93	8	2	0.5	8
8.43				4
8.53	5	2	1	10
8.58	20	5	2	200
8.63	30	5	4	600
10.83	10	3	1.3	39
11.03				4
12.33	10	4	1	40
13.47				3
14.03				10
14.23	20	3	2	120
14.83				2
15.23	10	4	1	40
15.24				2
15.24				2
15.25				2
15.54				2
15.58				2
17.53	8	2	0.5	8
18.13	3	1	1	3
18.33	10	5	2	100
19.13	10	10	2	200
19.43	1	1	1	1
19.83	1	1	1	1
20.77	10	15	3	450
21.53	3	1	1	3
21.93	30	7	3	630
22.18	5	5	2	50
22.23	5	2	1	10
26.4	20	2	1	40
26.43	2	2	1	4
Total				**6024**

[a] Distance along the Sharon Escarpment (A–A′, shown in Fig. 2).
[b] Volumes are calculated from field measurements of landslide scar length, height and estimated thickness. In cases of small landslides bulk volumes were estimated directly.

sampling intervals achieved with the LiDAR scans, storm-induced instability at Olga N, Herzlia and Gaash appears to have ceased by days 33, 38 and 191 after the storm, respectively. At Olga S, which is the best sampled site, post-storm activity persisted until day 119 after the storm, with a notable activity peak between days 96 and 119 (Fig. 4). While no significant failure events were documented at Olga S after day 119, open cracks in the upper cliff-face sections

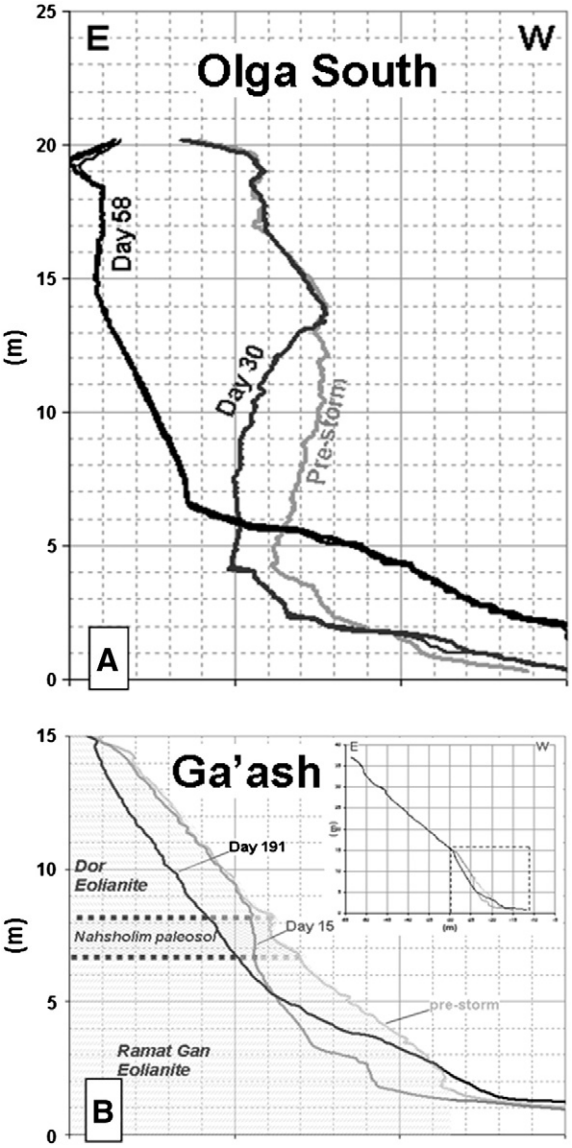

Figure 7. Cross sections of cliff-face geometries representing the post-storm up-cliff migration of cliff collapse in response to wave-driven basal erosion at Olga S (A) and Ga'ash (B).

https://doi.org/10.1016/j.yqres.2013.04.004 Published online by Cambridge University Press

indicate that increased post-storm cliff instability persists at this site even 1 year after the storm. Longer time scales for cliff response to basal instability induced by the storm most-likely occur at the Apollonia site, where minor post-storm cliff-face erosion was observed although 2–3 m basal notches were carved during the storm.

Lack of additional 'strong' post-storm weather events suggests that the peak in gravitational collapse events between days 96 and 119 may be attributed to either: 1) the effective time scale for up-cliff migration of gravitational instability induced by the overhang geometry carved during the storm (Fig. 7), and/or 2) coincident soil moisture saturation of the cliff section during the Mediterranean winter season. We also find no relation between the timing of the slope-failure events and their specific failure mechanism (e.g., rockfall/slumping). Thus, at this stage, the physical parameters controlling the time scales of post-storm cliff collapse remain less constrained and are the focus of ongoing research.

Summed together, cliff-face basal erosion driven by direct wave impact during the storm amounted to 1412 m^3 at all the LiDAR monitored sites. Post-storm gravitational cliff collapses that followed amounted to 3229 m^3. Thus, 70% of the total cliff-face erosion within the LiDAR sites during the 2010–2011 season occurred as gravitational response of the cliff to wave-cut basal instability. The LiDAR data also reveal a positive correlation between the volumes of the individual post-storm gravity-driven cliff collapses and the volumes of the syn-storm basal cliff-face erosion that occurred directly below them (Fig. 8). While this correlation is based on relatively few observations, it may provide a basis for predictive relations between syn-storm erosion and subsequent slope-failure volumes in appropriate environments.

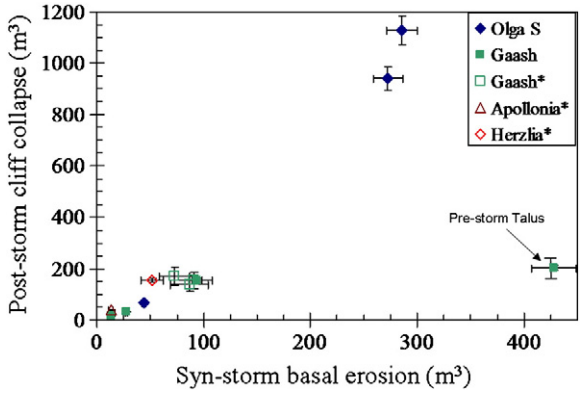

Figure 8. Volume of the individual post-storm cliff-collapse events (y-axis) vs. the volume of syn-storm basal erosion directly below them (x-axis). All volumes are derived from the LiDAR difference maps (Table 1). Closed symbols mark collapse events for which both storm and post-storm volumes could be directly measured from the LiDAR difference maps with uncertainty bounds of ±6%. Open symbols mark collapse events for which wave-driven erosion was partially obscured by talus from the post-storm collapse events. In these cases, the volume of storm erosion below the post-storm collapse was estimated by extrapolation between syn-storm erosion exposed and preserved on both sides of the post-storm talus. Uncertainty bounds for these extrapolated syn-storm volume estimates is ±20% (x-axis). The outlier in the bottom right occurs within a large pre-storm talus pile at the Ga'ash site (Fig. S3), whereas all other data points represent cliff-face erosion events.

4.2. Erosion characteristics of the Sharon Escarpment

Process-oriented approaches to coastal-cliff retreat typically consider two primary modes of erosion (e.g., Dong and Guzzetti, 2005): 1) gradual 'grain-by-grain' cliff-face erosion driven through a suite of eolian and aqueous processes, and 2) cliff-face erosion by discrete slope failure events. At the LiDAR sites as well as along the entire Sharon Escarpment, 2010–2011 erosional cliff-face scars are marked by a "fresh" non-crusted field appearance that contrasts the darker toned (brown) 'crusted' field appearance, which increases with time along stable cliff sections. Volumetrically significant 'grain-by-grain' erosion would not allow for this observed correlation between the degree of crusting on the cliff face and the duration of its stability. Thus, it appears that that landwards retreat in the Sharon Escarpment is primarily driven by the latter mode of erosion, namely discrete slope-failure events.

A total of 101 discrete cliff-face erosional scars associated with the 2010–2011 season occur along the 30-km length of the Sharon Escarpment (LiDAR sites and field transect, Tables 1 and 2, respectively). The size–frequency distribution of erosion associated with these scars in log-log space is close to linear with a scaling exponent of $\beta = -1.02$ (Fig. 9). This β value is comparable to that found in other gravity-driven slope failures triggered by either earthquakes or rainfall in natural inland environments ($\beta = -1.1$ to -1.4; e.g., Guzzetti et al., 2003; Malamud et al., 2004; Kanari, 2008; Brunetti et al., 2009) and in scaled sandbox experiments ($\beta = -1.1$; Katz and Aharonov, 2006). The similarity in size–frequency distribution suggests that like slope failures in other gravitationally unstable environments, sea-cliff erosion along the Sharon Escarpment during the 2010–2011 season can be effectively regarded as a gravitationally driven process in geologically weak material.

4.3. The role of strong storms in the longer-term evolution of the escarpment

Previously determined cliff retreat rates along the Sharon Escarpment, which have been locally constrained at up to decadal time scales, range between 0.1 and 0.5 m/yr (Zviely and Klein, 2004 and references therein). Extrapolation of such retreat rates across the 30-km-length of the Sharon Escarpment (average cliff height of 18 m, i.e., cliff-face area of 540,000 m^2) would translate to annually averaged cliff-scale erosion volumes of 54,000–270,000 m^3/yr. These averaged annual erosion volumes are up to an order of magnitude higher than the total 12,200 ± 3300 m^3 of cliff-face erosion measured along the entire escarpment during the December 2010 storm and the year that followed. This discrepancy between implied and measured cliff-scale annual erosion volumes may be associated in part with the simplified extrapolation of locally constrained retreat rates to the entire cliff line, which can result in overestimation of cliff-scale erosion rates (e.g., Quinn et al., 2009). And yet, our results suggest that in addition to being limited to less than 4% of the escarpment length, the erosional effects of the December 2010 storm are also limited by volume compared to the

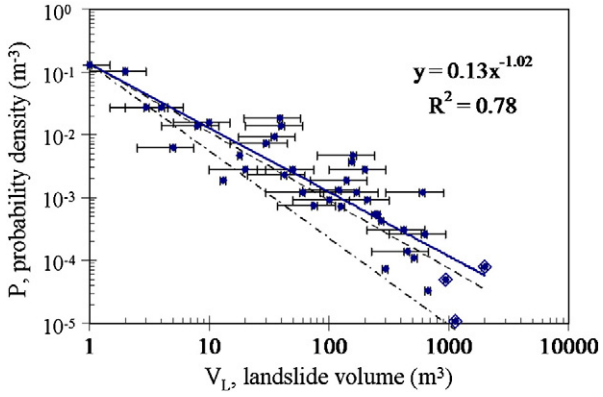

Figure 9. Probability density of landslide volumes (P) as a function of landslide volume (V_L) for the 101 discrete erosion events documented along the Sharon Escarpment during the 2010–2011 season. Uncertainties in volumes are ±6 and 50% for LiDAR measured and field constrained erosion events, respectively. Double framed symbols mark erosion events that occurred at local capes. Dashed lines mark the range of β slopes previously determined for other gravity-driven slope-failures in natural inland environments, i.e., −1.1 & −1.4 (Guzzetti et al., 2003; Malamud et al., 2004; Kanari, 2008; Brunetti et al., 2009).

https://doi.org/10.1016/j.yqres.2013.04.004 Published online by Cambridge University Press

average annual cliff-scale erosion volumes of the Sharon Escarpment estimated from previously published retreat rates. Similar conclusions regarding the non-exceptional role of individual strong events have been previously suggested in other weakly lithified coastal cliff environments: e.g., the till-dominated UK coasts (Quinn et al., 2009; Brooks and Spencer, 2010) and in Pont Loma, southern California (Young et al., 2011).

In contrast to the apparently non-exceptional cliff-scale erosion volume of the December 2010 storm, we identify a unique spatial 'fingerprint' in the spatial distribution of erosional activity associated with the storm. Capes, which compose up to 10% of the Sharon Escarpment length, accommodated 40% of the 2010–2011 slope-failure events larger than 500 m^3 and 33% of the total cliff-face erosional volume documented (Fig. 9). Assuming that this observed spatial pattern of erosional activity is characteristic of strong storms, we suggest that such storms may have a key role in impeding the development of cape–embayment cliff-line geometry and in maintaining cliff-scale linearity along the Sharon Escarpment.

The observed spatial pattern of erosion associated with the December 2010 storm and the year that followed could conceivably be associated with the partly submerged boulder fronts that typically occur about the capes as effective wave breakers (Fig. 3). Cliff-base shielding from direct wave impact during 'regular' storms by these m-high boulder fronts is likely reduced during strong storms with exceptionally high waves. And thus, we postulate that 'regular' storms may be driving erosion and retreat along exposed cliff sections void of such natural wave breakers, and that only 'strong' storms (e.g., the December 2010 storm) are capable of triggering cliff erosion along shielded cliff sections such as capes.

4.4. Broader implications

The erosion process of weakly lithified sea cliffs through discrete gravity-driven slope failure events is composed of three distinguishable and sequential erosion 'types' (Wiseman et al., 1981): *Type 1* is 'Triggering' activity, in which erosion of the basal parts of the cliff face by direct wave impact (scouring) induces increased gravitational instability in the cliff face above. *Type 2* is 'Primary Erosion', in which up-cliff migration of basal instability occurs in response to type 1 erosion through discrete slope-failure events. Type 2 erosion results in disintegrated material piled up at the cliff base as talus and/or boulders. *Type 3* is 'Secondary Erosion', in which pre-existing talus piles are removed through wave scouring and the cliff base is re-exposed to type 1 activity. Triggering, primary and secondary erosion comprised 12%, 57% and 31% of the total erosion associated with the December 2010 storm at the LiDAR monitored sites (Table 3).

These observations also relate to recently emerging predictive hazard mitigation efforts in coastal cliff environments (e.g., Quinn et al., 2009, 2010; Castedo et al., 2012) as they allow us to place quantitative constraints on key spatial and temporal aspects of post-storm erosional cliff activity. We identify a predictive association between all catastrophic slope-failure events at the monitored sites and significant basal erosion that precedes and triggers them (Fig. 8). This triggering wave-driven basal erosion is measurable by ground-based LiDAR techniques. Post-storm slope-failure events in the Sharon Escarpment continued to occur several months after the formation of the basal instability that triggered them (Fig. 4). Destabilized cliff sections that remain at elevated risk of failure following significant basal erosion at the Olga S and Apollonia sites indicate that longer time scales for gravitational cliff response may also be involved. Recognizing that the temporal aspect of post-storm gravitational cliff collapse remains somewhat loosely constrained, we propose that post-storm sea-cliff erosion along Israel's Mediterranean coast and in other similar eolianite environments may be treated as a gravity-driven threshold problem in geologically weak material.

Table 3
Summary of syn-storm talus and cliff-base erosion and post-storm erosion at the five LiDAR sites.

	Olga N (m^3)	Olga S (m^3)	Ga'ash (m^3)	Apollonia (m^3)	Herzliya (m^3)	Total (m^3)	%
Syn-storm talus erosion	0	140	2090	0	555	2785	31
Syn-storm cliff base erosion	–[a]	933	0	179	0	1102[a]	12
Post Storm erosion	1985	2176	721	63	155	5100	57
Total	1985	3249	2811	242	710	8997	100

[a] Field evidence indicates that significant cliff-face basal erosion occurred at this site. However, lack of pre-storm LiDAR data at Olga N precludes robust quantitative estimation of its volume. Thus, the total cliff-face basal erosion for all sites should be regarded as a minimum bound.

5. Conclusions

Characterization of changes in sea-cliff morphology through high resolution ground-based LiDAR campaigns allowed us to derive quantitative insights into the primary mechanisms that govern erosion and inland retreat of Israel's Mediterranean weakly cemented eolianite cliff line during a strong winter storm with up to 12–14 m waves (10–20 years recurrence interval) and the year that followed. In a more general sense, this study effectively documented an instantaneous perturbation in cliff stability induced by the storm, peak post-storm cliff erosion, and subsequent relaxation of the system down to transient stability.

We identified two phases of cliff-face erosion associated with the storm: 1) Basal scouring of the cliff face through direct wave impact during the storm resulting in formation of over steepened/overhanging cliff-base geometry, and 2) subsequent post-storm gravitational response of the upper cliff face above to the basal instability formed during the storm. Post-storm slope-failure events persisted up 4 months after the storm and amounted to 70% of the total cliff-face erosion volume documented during the study period. A predictive association was identified between post-storm catastrophic cliff-failure events and measurable wave-driven basal scouring of the cliff face directly below. Our results support the view of post-storm sea-cliff erosion in such similar coastal environments as a gravity-driven process in geologically weak material. Cliff-face erosion along the entire 30-km-long Sharon Escarpment during the storm and the year that followed amounted to 12,200 $\pm$ 3300 m^3 and was locally significant with up to 8 m of catastrophic cliff-normal retreat recorded in places. However, less than 4% of the escarpment length was affected by this storm-related erosion, which appears to be also limited by volume compared to average cliff-scale volumetric erosion rate of the Sharon Escarpment implied from previously published decadal-scale retreat rates. Thus, our results do not support a direct straight-forward causal association between strong storm events and exceptional escarpment-scale retreat. Nonetheless, the preferential occurrence of storm-related erosion about capes, suggests a possible role for such high-energy storms in buffering the development of cape–embayment cliff-line geometry along the Sharon Escarpment.

Supplementary data to this article can be found online at http://dx.doi.org/10.1016/j.yqres.2013.04.004.

Acknowledgments

Neomie Shahar (Geological Survey of Israel) performed the LiDAR post-processing as well as supported data acquisition in the field. Her contribution to the success of this work is invaluable. We thank Ori Shapira from Israel's Nature and Parks Authority (NPA) for his cooperation and assistance in the field and Hagi Yohanan (NPA) for facilitating access to the Apollonia site. Comments by three anonymous reviewers as well as insightful comments from the editors significantly contributed to the clarity and quality of the manuscript.

References

Allan, J.C., Komar, P.D., 2002. Extreme storms on the Pacific Northwest Coast during the 1997–98 El Niño and 1998–99 La Ninia. Journal of Coastal Research 18, 175–193.

Almagor, G., 2005. The Mediterranean coast of Israel. Geological Survey of Israel, Report, GSI/13/02.

Arkin, Y., Michaeli, L., 1985. Short- and long-term erosional processes affecting the stability of Mediterranean coastal cliffs of Israel. Engineering Geology 21, 153–174.

Barlow, J., Lim, M., Rosser, N., Petley, D., Brain, M., Norman, E., Geer, M., 2012. Modeling cliff erosion using negative power law scaling of rockfalls. Geomorphology 139–140, 416–424.

Benumof, B.T., Storlazzi, C.D., Seymour, R.J., Griggs, G.B., 2000. The relationship between incident wave energy and seacliff erosion rates: San Diego County, California. Journal of Coastal Research 16 (4), 1162–1178.

Bray, M.J., Hoke, J.M., 1997. Prediction of soft-cliff retreat with accelerating sea-level rise. Journal of Coastal Research 13, 453–467.

Brooks, S.M., Spencer, T., 2010. Temporal and spatial variations in recession rates and sediment release from soft rock cliffs, Suffolk coast, UK. Geomorphology 124, 26–41.

Brooks, S.M., Spencer, T., Boreham, S., 2012. Deriving mechanisms and thresholds for cliff retreat in soft-rock cliffs under changing climates: rapidly retreating cliffs of the Suffolk coast, UK. Geomorphology 153–154, 48–60.

Brunetti, M.-T., Guzzetti, F., Rossi, M., 2009. Probability distributions of landslide volumes. Nonlinear Processes in Geophysics 16, 179–188.

Budetta, P., 2011. Stability of an undercut sea-cliff along a Cilento coastal stretch (Campania, Southern Italy). Natural Hazards and Earth System Sciences 56, 233–250.

Budetta, P., Galietta, G., Santo, A., 2000. A methodology for study of the relation between coastal cliff erosion and the mechanical strength of soils and rock masses. Engineering Geology 56, 243–256.

Castedo, R., Murphy, W., Lawrence, J., Paredes, C., 2012. A new process-response coastal recession model of soft rock cliffs. Geomorphology 177–178, 128–143.

Collins, B.D., Sitar, N., 2008. Processes of coastal bluff erosion in weakly lithified sands, Pacifica, California, USA. Geomorphology 97, 483–501.

Collins, B.D., Sitar, N., 2011. Stability of steep slopes in cemented sands. Journal of Geotechnical and Geoenvironmental Engineering 137, 43–51.

Dong, P., Guzzetti, F., 2005. Frequency-size statistics of coastal soft cliff erosion. Journal of Waterway, Port, Coastal, and Ocean Engineering-ASCE 131 (1), 37–42.

Engelmann, A., Neber, A., Frenchen, M., Boenigk, W., Ronen, A., 2001. Luminescence chronology of Upper Pleistocene and Holocene aeolianites from Netanya South Sharon Coastal Plain, Israel. Quaternary Science Reviews 20, 799–804.

Ferreira, O., 2005. Storm groups versus extreme single storms: predicted erosion and management consequences. Journal of Coastal Research 42, 221–227.

Frenchen, M., Dermann, B., Boenigk, W., Ronen, A., 2001. Luminescence chronology of aeolianites from the section at Givat Olga Coastal Plain of Israel. Quaternary Science Reviews 20, 805–809.

Frenchen, M., Neber, A., Dermann, B., Tsatskin, A., Boenigk, W., Ronen, A., 2002. Chronostratigraphy of aeolianites from the Sharon Coastal Plain of Israel. Quaternary International 89, 31–44.

Frydman, S., 2011. Characterizing the geotechnical properties of natural, Israeli, partially cemented sands. Geomechanics and Engineering 3 (4).

Goldreich, Y., 2003. The Climate of Israel: Observation, Research, and Application. Kluwer Academic/Plenum Publishers, New York.

Guzzetti, F., Reichenbach, P., Wieczorek, G.F., 2003. Rockfall hazard and risk assessment in the Yosemite Valley, California, USA. Natural Hazards and Earth System Sciences 3, 491–503.

Gvirtzman, G., Shachnai, E., Bakler, N., Ilani, S., 1984. Stratigraphy of the Kurkar Group (Quarternary) of the coastal plain of Israel. Geological Survey of Israel, Current Research 1983-4. 70–82.

Hampton, M.A., 2002. Gravitational failure of sea cliffs in weakly lithified sediment. Environmental and Engineering Geoscience 8, 175–191.

Hansom, J.D., Barltrop, N.D.P., Hall, A.M., 2008. Modelling the processes of cliff-top erosion and deposition under extreme storm waves. Marine Geology 253, 36–50.

Hapke, C., Richmond, B., 2002. The impact of climatic and seismic events on the short-term evolution of sea cliffs based on 3-D mapping: Northern Monterey Bay, California. Marine Geology 187 (3–4), 259–278.

Jones, J.R., Cameron, B., Fisher, J., 1993. Analysis of cliff retreat and shoreline erosion: Thompson Island, Massachusetts, U.S.A. Journal of Coastal Research 9, 87–96.

Kanari, M., 2008. Evaluation of rockfall hazard to Qiryat Shemona — possible correlation to earthquakes. Geological Survey of Israel, Report GSI/24/2008.

Katz, O., Aharonov, E., 2006. Landslides in vibrating sand-box: what controls types of slope-failure and frequency magnitude relations? Earth and Planetary Science Letters 247, 280–294.

Katz, O., Hecht, H., Petranker, G., Almog, E., 2007. Retreat rate of the Israeli coastal cliff and its estimated location at 2100. (in Hebrew, abstract in English) Geological Survey of Israel, Report: GSI/21/07.

Klein, M., Lichter, M., 2007. Statistical analysis of recent Mediterranean sea-level data. Geomorphology 107, 3–9.

Kogure, T., Matsukura, Y., 2010. Critical notch depths for failure of coastal limestone cliffs: case study at Kuro-shima Island, Okinawa, Japan. Earth Surface Processes and Landforms 35, 1044–1056.

Kogure, T., Hisashi, A., Akira, M., Takashi, H., Yukinori, M., 2006. Effect of the development of notches and tension cracks on instability of limestone coastal cliffs in the Ryukyus, Japan. Geomorphology 80, 236–244.

Komar, P.D., Shih, S.H., 1993. Cliff erosion along the Oregon Coast: a tectonic-sea level imprint plus local controls by beach processes. Journal of Coastal Research 9, 747–765.

Lambeck, K., Purcell, A., 2005. Sea-level change in the Mediterranean Sea since the LGM: model predictions for tectonically stable areas. Quaternary Science Reviews 24, 1969–1988.

Lee, E.M., Hall, J.W., Meadowcroft, I.C., 2001. Coastal cliff recession: the use of probabilistic prediction methods. Geomorphology 40, 253–269.

Lee, E.M., Meadowcroft, I.C., Hall, J.W., Walkden, M., 2002. Coastal landslide activity: a probabilistic simulation model. Bulletin of Engineering Geology and the Environment 61, 347–355.

Lim, M., Petley, D.N., Rosser, N.J., Allison, R.J., Long, A.J., Pybus, D., 2005. Combined digital photogrammetry and time-of-flight laser scanning for monitoring cliff evolution. The Photogrammetric Record 20, 109–129.

Lim, M., Rosser, N.J., Allison, R.J., Petley, D.N., 2010. Erosional processes in the hard rock coastal cliffs at Staithes, North Yorkshire. Geomorphology 114, 12–21.

Lowe, J.A., Howard, T., Pardaens, A., Tinker, J., Holt, J., Wakelin, S., Milne, G., Leake, J., Wolf, J., Horsburgh, K., Reeder, T., Jenkins, G., Ridley, J., Dye, S., Bradley, S., 2009. UK Climate Projections Science Report: Marine and Coastal Projections. Met Office Hadley Centre, Exeter, UK978-1-906360-03-0.

Malamud, B.D., Turcotte, D.L., Guzzetti, F., Reichenbach, P., 2004. Landslide inventories and their statistical properties. Earth Surface Processes and Landforms 29, 687–711.

Marques, F.M.S.F., 2008. Magnitude-frequency of sea cliff instabilities. Natural Hazards and Earth System Sciences 8, 1161–1171. http://dx.doi.org/10.5194/nhess- 8-1161-2008.

Mills, J.P., Buckley, S.J., Mitchell, H.L., Clarke, P.J., Edwards, S.J., 2005. A geomatics data integration technique for coastal change monitoring. Earth Surface Processes and Landforms 30, 651–664.

Moore, L.J., Griggs, G.B., 2002. Long-term cliff retreat and erosion hotspots along the central shores of the Monterey Bay National. Marine Sanctuary. Marine Geology 181, 265–283.

Olsen, M.J., Johnstone, E.A., Driscoll, N., 2011. Seacliff erosion analysis using 3D laser scanning. Geological Society of America Abstracts with Programs 43 (5), 618.

Porat, N., Wintle, A.G., Rite, M., 2004. Mode and timing of kurkar and hamra formation, central coastal plain, Israel. Israel Journal of Earth Sciences 53, 13–25.

Quinn, J.D., Philip, L.K., Murphy, W., 2009. Understanding the recession of the Holderness Coast, east Yorkshire, UK: a new presentation of temporal and spatial patterns. Quarterly Journal of Engineering Geology & Hydrogeology 42, 165–178. http://dx.doi.org/10.1144/1470-9236/08-032.

Quinn, J.D., Rosser, N.J., Murphy, W., Lawrence, J.A., 2010. Identifying the behavioural characteristics of clay cliffs using intensive monitoring and geotechnical numerical modeling. Geomorphology 120, 107–122.

Regard, V., Dewez, T., Bourlès, D.L., Anderson, R.S., Duperret, A., Costa, S., Leanni, L., Lasseur, E., Pedoja, K., Maillet, G.M., 2012. Late Holocene seacliff retreat recorded by 10Be profiles across a coastal platform: Theory and example from the English Channel. Quaternary Geochronology 11, 87–97.

Richards, K.S., Lorriman, N.R., 1987. Basal erosion and mass movement. In: Anderson, M.G., Richards, K.S. (Eds.), Slope Stability. Wiley, New York, pp. 331–357.

Rosser, N.J., Petley, D.N., Lim, M., Dunning, S.A., Allison, R.J., 2005. Terrestrial laser scanning for monitoring the process of hard rock coastal cliff erosion. Quarterly Journal of Engineering Geology and Hydrogeology 38, 363–375.

Sallenger Jr., A.H., Krabill, W., Brock, J., Swift, R., Manizade, S., Stockdon, H., 2002. Sea-cliff erosion as a function of beach changes and extreme wave runup during the 1997–1998 El Niño. Marine Geology 187, 279–297.

Shalev, E., Lazar, A., Wollman, S., Kington, S., Yechieli, Y., Gvirtzman, H., 2009. Biased monitoring of fresh water–salt water mixing zone in coastal aquifers. Ground Water 47, 49–56.

Sivan, D., Wdowinski, S., Lambeck, K., Galili, E., Raban, A., 2001. Holocene sea-level changes along the Mediterranean coast of Israel, based on archaeological observations and numerical model. Palaeogeography, Palaeoclimatology, Palaeoecology 167, 101–117.

Sivan, D., Raban, K., Lambeck, T.A., Porath, Y., Shirman, B., 2004. Ancient coastal wells of Caesarea Maritima, Israel, an indicator for relative sea level changes during the last 2000 years. Earth and Planetary Science Letters 222, 315–330.

Steers, J.A., Stoddart, D.R., Bayliss-Smith, T.P., Spencer, T., Durbridge, P.M., 1979. The storm surge of 11 January 1978 on the east coast of England. The Geographical Journal 145, 192–205.

Sunamura, T., 1982. A predictive model for wave-induced cliff erosion, with application to Pacific coasts of Japan. Journal of Geology 167–178.

Sunamura, T., 1992. Geomorphology of Rocky Coasts. John Wiley & Sons.

Teixeira, S.B., 2006. Slope mass movements on rocky sea-cliffs: a power law distributed natural hazard on the Barlavento Coast, Algarve, Portugal. Continental Shelf Research 26, 1077–1091.

Thorne, C., Evans, E.P., Penning-Rowsell, E.C. (Eds.), 2007. Future Flood and Coastal Erosion Risks. Thomas Telford, London.

Tsoar, H., 2000. Geomorphology and paleogeography of sands dunes that have formed along the kurkar ridges in the coastal plans of Israel. Israel Journal of Earth Sciences 49, 189–196.

Williams, W.W., 1956. An East Coast survey: some recent changes in the coast of East Anglia. The Geographical Journal 122, 317–327.

Wiseman, C., Hayati, G., Frydman, S., 1981. Stability of heterogeneous sandy coastal cliff. Proceeding, Soil mechanics and foundation engineering 10th conference, Stockholm, 11/59. AA Balkema, Rotterdam, pp. 568–574.

Wolman, M.G., Miller, J.P., 1960. Magnitude and frequency of forces in geomorphic processes. Journal of Geology 68, 54–74.

Yaalon, D.H., 1967. Factors affecting the lithification of eolianite and interpretation of its environmental significance in the coastal plain of Israel. Journal of Sedimentary Petrology 37, 1189–1199.

Young, A.P., Ashford, S.A., 2008. Instability investigation of cantilevered seacliffs. Earth Surface Processes and Landforms 33, 1661–1677.

Young, A.P., Flick, R.E., Gutierrez, R., Guza, R.T., 2009a. Comparison of short-term seacliff retreat measurement methods in Del Mar, California. Geomorphology 112, 318–323.

https://doi.org/10.1016/j.yqres.2013.04.004 Published online by Cambridge University Press

Young, A.P., Guza, R.T., Flick, R.E., O'Reilly, W.C., Gutierrez, R., 2009b. Rain, waves, and the short-term evolution of composite seacliffs in southern California. Marine Geology 267, 1–7.
Young, A.P., Olsen, M.J., Driscoll, N., Flick, R.E., Gutierrez, R.T., Johnston, E., Kueste, R., 2010. Comparison of airborne and terrestrial Lidar estimates of sea cliff erosion in Southern California. Photogrammetric Engineering and Remote Sensing 76, 421–427.
Young, A.P., Guza, R.T., Oreilly, W.C.O., Flick, R.E., Gutierrez, R., 2011. Short-term retreat statistics of a slowly eroding coastal cliff. Natural Hazards and Earth System Sciences 11, 205–217.
Zhang, K., Douglas, B.C., Leatherman, S.P., 2004. Global warming and coastal erosion. Climate Change 64, 41–58.
Zviely, D., Klein, M., 2004. Coastal cliff retreat rates at Beit-Yannay, Israel, in the 20th century. Earth Surface Processes and Landforms 29, 175–184.

https://doi.org/10.1016/j.yqres.2013.04.004 Published online by Cambridge University Press